Earth and Planetary Science Letters 297 (2010) 607–615

Contents lists available at ScienceDirect

Earth and Planetary Science Letters

journal homepage: www.elsevier.com/locate/epsl

Insights into the kinematics of a volcanic caldera drop: Probabilistic finite-source inversion of the 1996 Bárdarbunga, Iceland, earthquake

Andreas Fichtner [a,*], Hrvoje Tkalčić [b]

[a] Department of Earth Sciences, Utrecht University, Utrecht, The Netherlands
[b] Research School of Earth Sciences, The Australian National University, Canberra, Australia

ARTICLE INFO

Article history:
Received 13 July 2009
Received in revised form 2 July 2010
Accepted 7 July 2010
Available online 6 August 2010

Editor: R.D. van der Hilst

Keywords:
volcanic caldera
Bárdarbunga
Iceland
finite-source inversion
spectral-element method
seismology

ABSTRACT

The accurate modelling and prediction of volcanic eruptions depends critically on information concerning the interaction between the caldera and the underlying magma chamber. Knowledge concerning the kinematics of a caldera in the course of an eruption is therefore essential. Here we provide detailed seismological constraints on the kinematics of a volcanic caldera drop and the geometry of a caldera ring fault. For this we performed a finite-source inversion of the September 29, 1996 Bárdarbunga, Iceland, earthquake that was caused by caldera subsidence. Our methodology is based on spectral element simulations of seismic wave propagation through a realistic model of the Icelandic crust and upper mantle. A particularly robust feature is the initiation of the rupture in the north-western part of the ring fault that is about 10 km in diameter. From there it spread to the other fault segments within about 3 s. Without invoking super-shear propagation sensu stricto, we can explain this unusually fast rupture propagation by the triggering of fault segments through P waves that propagated across the caldera. Our results favour outward-dipping fault segments in the western half of the ring fault, while the eastern half is preferentially inward-dipping. This variability may reflect structural heterogeneities or an irregular magma chamber geometry. The individual segments of the caldera ring fault radiated approximately equal amounts of energy. This indicates that the caldera dropped coherently as one single block.
The work presented here is intended to aid in the design of realistic models of magma chamber and caldera dynamics.

1. Introduction

Observational constraints on caldera kinematics are essential for the design of realistic models of volcano dynamics and thus for the assessment of volcanic hazard (e.g. Druitt and Sparks, 1984; Martí et al., 2000; Geyer et al., 2006; Folch and Martí, 2009).

In recent years, much progress was made in our understanding of the geometrical features of volcanic calderas and their relation to rheology and magma chamber properties. Geshi et al. (2002) directly observed the formation of an outward-dipping caldera ring fault after the eruption of Miyakejima Volcano, Japan. Rymer et al. (1998) report a natural cross-section at Masaya Volcano, Nicaragua, where outward-dipping faults are exposed. Branney (1995) explores ice-melt collapse pits, mining subsidence structures and calderas, concluding that reverse faults are likely to form during collapse. Near-surface inward-dipping faults form subsequently due to peripheral extension and scarp collapse, though accounting for only a small portion of the total downward movement. Seismologic evidence for reverse ring faults is provided by hypocentre distributions in several volcanic areas. These include Mt. St. Helens, USA (Scandone and Malone, 1985), Rabaul, Papua New Guinea (Mori and McKee, 1987), Pinatubo, Philippines (Mori et al., 1996) and Mammoth Mountain, USA (Prejean et al., 2003). Analogue models of caldera collapse confirm the formation of outward-dipping reverse faults in the central part of the caldera followed by the gravity-driven appearance of peripheral normal faults (e.g. Roche et al., 2000; Acocella, 2007).

While the geometrical features of calderas have been studied in detail, there are still few constraints on the kinematics of the actual caldera drop. The principal objective of this study therefore is to fill this gap using seismic data. For this we analyse broadband seismograms recorded by the temporary Iceland HOTSPOT seismic experiment stations (Foulger et al., 2001) in order to infer the finite source rupture process of the September 29, 1996, Bárdarbunga earthquake that was caused by a sudden caldera subsidence along a pre-existing ring fault. By means of a probabilistic source inversion we obtain information on the rupture time and relative magnitude distributions along the ring fault, as well as on the inclination of different fault segments.

Bárdarbunga volcano, located under the Vatnajökull glacier in SE Iceland, has long been recognised as the source of anomalous non-

* Corresponding author.
E-mail addresses: fichtner@geo.uu.nl (A. Fichtner), hrvoje.tkalcic@anu.edu.au (H. Tkalčić).

0012-821X/$ – see front matter © 2010 Elsevier B.V. All rights reserved.
doi:10.1016/j.epsl.2010.07.013

double-couple (NDC) earthquakes (Ekström, 1994). The most recent NDC event at Bárdarbunga occurred on September 29, 1996, one day before a major subglacial fissure eruption. A detailed waveform analysis of this $M_w = 5.6$ earthquake revealed that its point source moment tensor is characterised by a dominant compensated linear vector dipole and a small double-couple component (Nettles and Ekström, 1998 Tkalčić et al. (2009) found an insignificant isotropic component that is unusual for large volcanic events. A likely tectonic explanation for the anomalous nature of the Bárdarbunga events, including the one in 1996, involves the drop of the volcanic caldera along an outward-dipping ring fault structure (Ekström, 1994; Nettles and Ekström, 1998). This interpretation is supported by aftershock locations (Konstantinou et al., 2000) and the frequent observation of outward-dipping ring faults associated with caldera subsidence.

This paper is organised as follows: We start with the description of a three-dimensional (3D) model of the Icelandic crust and uppermost mantle, which is an essential ingredient of a successful seismic source inversion. Using vertical-component recordings of an $M_L \approx 3.3$ aftershock, we then verify the accuracy of the structural model. That finite-source effects can indeed be observed in the waveforms of the mainshock follows from a point-source moment tensor inversion that can not simultaneously explain the data in different frequency bands. In a probabilistic finite source inversion we then obtain marginal probability distributions for the parameters rupture time, relative magnitude and subfault inclination angle. In the final paragraphs we discuss the results and their implications for the kinematics of a volcanic caldera drop.

2. Construction of the structural model

A kinematic source inversion requires that waveform differences between the observed and synthetic seismograms be dominated by finite-source effects. The synthetic seismograms therefore need to be computed with an accurate structural model (Graves and Wald, 2001). Such models have become available thanks to extensive studies of the Icelandic crust and upper mantle during the past decades (e.g. Båth, 1960; Tryggvason, 1962; Foulger et al., 2001; Allen et al., 2002). In this study we use a 3D model that is based on a spline interpolation of vertical profiles that were determined from receiver functions and surface wave dispersion data (Du and Foulger, 2001; Du et al., 2002; Du and Foulger, 2004). The profiles were found to be consistent with data from explosion seismology (Staples et al., 1997; Darbyshire et al., 1998; Foulger et al., 2003). In Fig. 1 we show the depth of the lower-crustal discontinuity (Moho) in the 3D model. Vertical slices through the 3D S wave speed model can be seen in Fig. 2.

We compute synthetic seismograms using a spectral-element discretisation of the elastic wave equation (Fichtner and Igel, 2008). The average grid spacing is 1.4 km, so that the complexities of the Icelandic crust can be accounted for correctly.

The combination of a well constrained structural model and highly accurate numerical simulations allows us to exploit the maximum amount of waveform information. This is a significant advantage over studies where either long-period regional surface waves (e.g. Konstantinou et al., 2003; Tkalčić et al. 2009) or far-field P waves (Nettles and Ekström, 1998) were used. Long-period ($T > 20s$) regional surface waves can be matched by a wide range of source mechanisms, especially in the case of shallow sources (Dziewonski et al., 1981). The inverse problem is therefore highly non-unique. Teleseismic body waves do not contain any near-field waveforms that are crucial for the correct determination of finite-source processes.

3. Verification of the structural model using aftershock data

To assess the quality of the structural model, we perform a moment tensor inversion for an $M_L \approx 3.3$ aftershock that occurred on October 1, 1996, in the northern part of the caldera fault. The relatively small magnitude of the aftershock justifies the point-source approximation. The results of the inversion allow us to estimate the extent to which the misfit between the observed and the synthetic seismograms is due to inaccuracies of the implemented velocity structure.

We base the moment tensor inversion on a Simulated Annealing algorithm (Kirkpatrick et al., 1983) that minimises the L_1 distance between data and synthetics. The choice of the L_1 norm - as opposed to the L_2 norm - reduces the influence of small time shifts between data and synthetics and therefore leads to more robust results. As data we use vertical-component recordings of 18 HOTSPOT stations, the locations of which are visualised in Fig. **1**. For this part of our study, we disregard horizontal-component data due to their low signal-to-noise ratio.

In this and all subsequent inversions, the data weighting is done as follows: (1) The weights are inversely proportional to the epicentral distance, so that the importance of the furthest stations is about 0.5 times the importance of the closest stations. This weighting is comparatively mild. It reduces the effects of unknown Earth structure and emphasises the near-field radiation. (2) We subdivide Iceland into 6 azimuthal sectors originating at the epicentre. The weights are

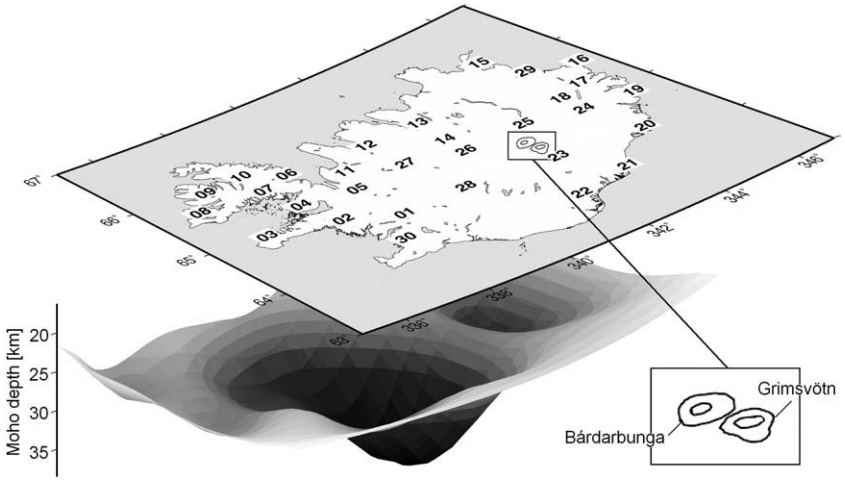

Fig. 1. Map showing the locations of the HOTSPOT seismic stations used in this study. The depth of the lower crustal discontinuity (Moho) as inferred by Du and Foulger (2001), Du et al. (2002) and Du and Foulger (2004) is shown below. The locations of Bárdarbunga and Grimsvötn volcanos are also displayed. The outer curves represent the central volcanoes and the inner curves mark the outlines of the calderas.

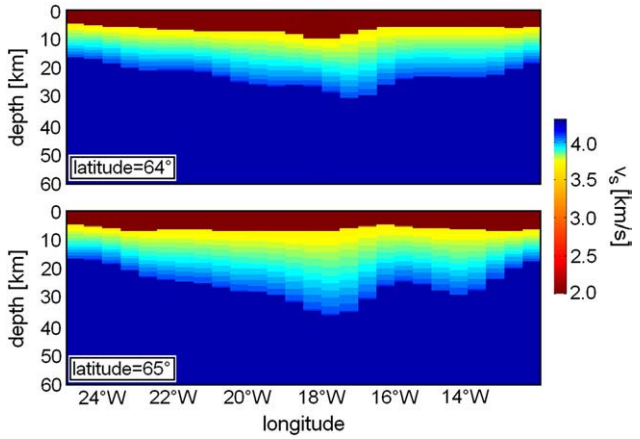

Fig. 2. Vertical slices through the 3D S wave speed model. The strongly variable thickness of the upper and lower crust is clearly visible. Note that the colour scale is not linear.

then inversely porportional to the number of stations in each sector. This minimises the effect of the uneven azimuthal station coverage.

To reduce the inherent non-uniqueness of a shallow-source moment tensor inversion (Dziewonski et al., 1981) we simultaneously consider 3 frequency bands, centred around 0.10 Hz, 0.15 Hz and 0.20 Hz, respectively. We found empirically that the simultaneous use of multiple frequency bands and relatively high frequencies strongly decreases the linear dependence of the Greens functions. Data with frequencies lower than 0.10 Hz do not add significant additional constraints on the moment tensor. Waveforms with frequencies higher than 0.20 Hz had to be excluded due to the micro-seismic noise. All 3 frequency bands were equally weighted in the inversion. Since the amplitudes of the seismic waveforms depend strongly on near-receiver structure, e.g. soil or ice, we only inverted normalised seismograms. Thus, we recover the source orientation but not the source magnitude.

The achieved waveform fit for the 0.20 Hz data is summarised in Fig. 3. The waveforms within and prior to the surface wave train are well recovered. Exceptions are the early smaller-amplitude arrivals at stations HOT15 and HOT29. This may be due to noise contamination. Similar arrivals at HOT13, HOT18 and HOT24 are, however, well modelled. For the data in the frequency bands around 0.15 Hz and 0.10 Hz we obtain waveform fits of equally good quality. The optimal moment tensor solution for the aftershock data is visualised in the lower-right corner of Fig. 3. Its CLVD component is 41%, meaning that the source is predominantly, but not exclusively, a double couple. This might be interpreted as slip along the caldera fault that was too small to activate the complete ring structure.

The fact that the details of the observed waveforms can be explained by a simple point source, indicates that the structural model is appropriate for vertical-component waveforms at frequencies below and including 0.20 Hz. A similar statement concerning horizontal-component recordings is currently not possible due to the low signal-to-noise ratio of the aftershock data.

4. The detectability of finite source effects

We repeat the moment tensor inversion outlined in the previous section for the mainshock data. Since it is to be expected that the source duration is on the order of the shortest period considered (5 s, Nettles and Ekström (1998)) we simultaneously invert for the moment rate function. The moment rate function is parameterised in terms of Lagrange polynomials with the collocation points located at the Gauss-Lobatto-Legendre (GLL) points. This produces a smoothly varying polynomial that does not suffer from strong oscillations near the edges of the considered time interval (Runge's phenomenon). We choose the polynomial degree 7 and set the values at the first and last

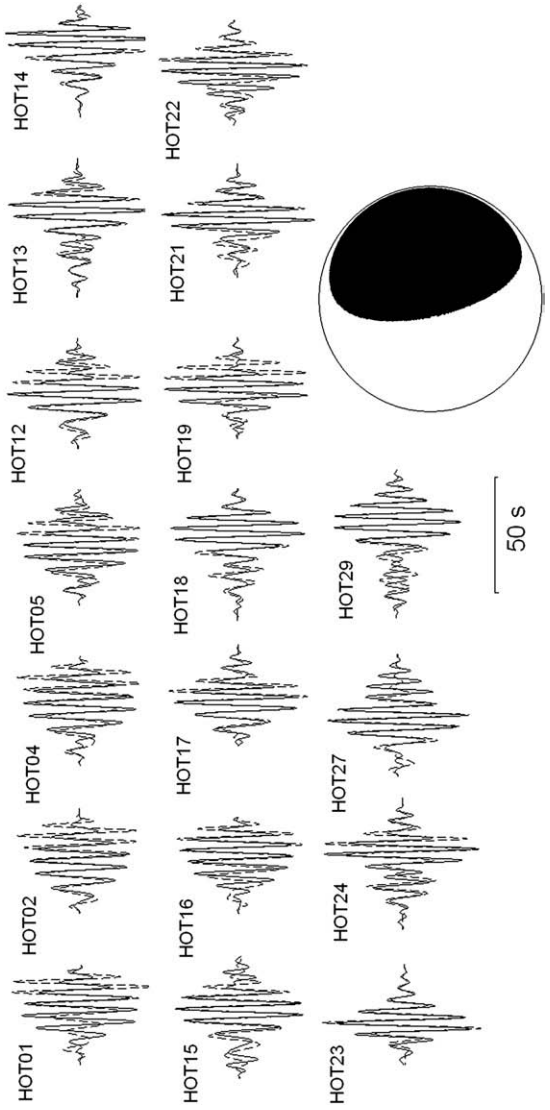

Fig. 3. Waveform comparison for the aftershock in the frequency band around 5 s. The data are plotted as solid curves and the synthetics as dashed curves. The waveform fit for the frequency bands around 0.15 Hz and 0.10 Hz is of comparable quality. The optimal moment tensor from the joint inversion in the three frequency bands is plotted on the lower right corner.

collocation points to zero. Thus, there are 7 free parameters for the source time function: the Lagrange polynomial coefficients for the 6 internal collocation points plus the variable interval length. These parameters are also found through Simulated Annealing.

The waveform fits resulting from the combined multi-frequency moment tensor plus moment rate function inversion are shown in Fig. 4 for the 0.20 Hz data. In general, the discrepancies between data and synthetics are larger than for the aftershock, despite the larger number of free parameters involved in the inversion. The optimal moment tensor solution, shown in the lower-right corner of Fig. 4, is close to the Centroid Moment Tensor solution and to that of the previous studies using regional waveforms an the deviatoric decomposition of the moment tensor (Nettles and Ekström, 1998; Tkalčić et al., 2009). Its CLVD component accounts for 71% of the total moment. From different runs of the Simulated Annealing algorithm we found that the moment rate function is not as well constrained as the moment tensor. We found source durations between 3 s and 8 s that explained the data equally well. The optimal moment rate function is displayed in Fig. 5. Its duration is 4.3 s but more than 90% of the total moment are released during the first 3.5 s.

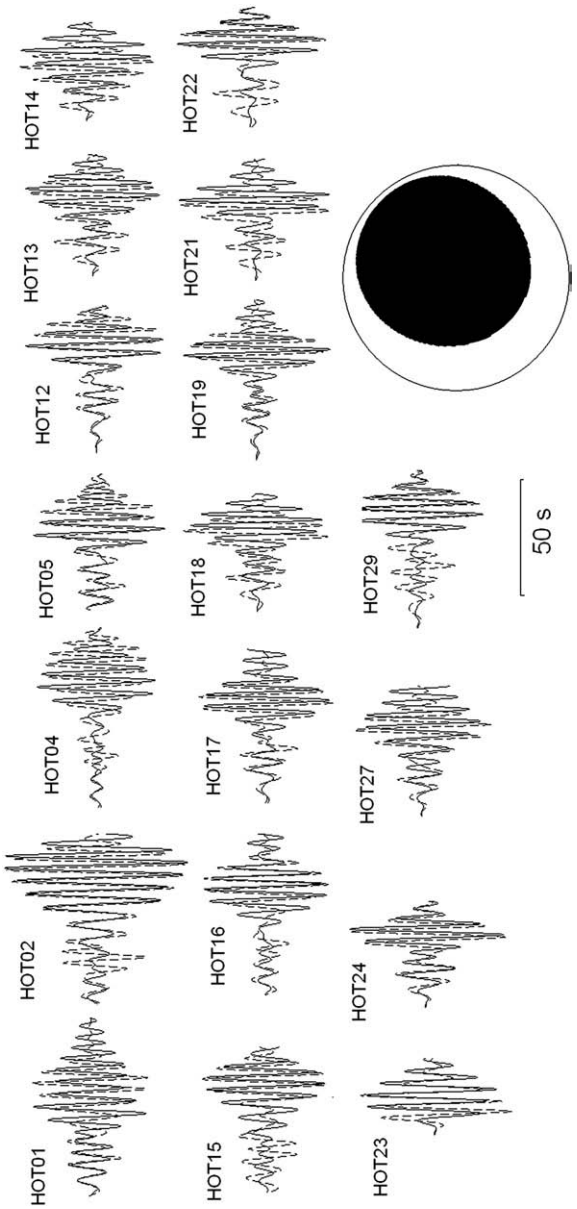

Fig. 4. Waveform comparison for the mainshock in the frequency band around 5 s. The synthetics for the optimal point-source moment tensor are plotted as dashed curves and the data as solid curves. Since the structural model was shown to be accurate, the disagreement between observed and synthetic waveforms indicates the influence of finite-source effects. The optimal moment tensor from the joint inversion in the three frequency bands is plotted on the lower right corner.

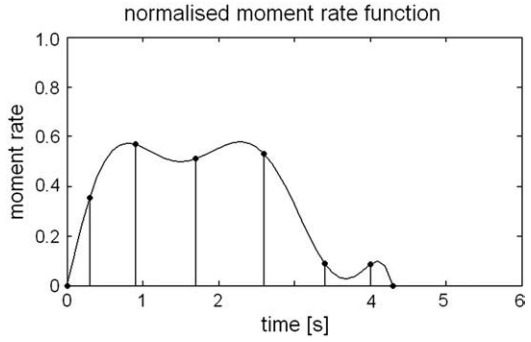

Fig. 5. Normalised moment rate function of the mainshock. The optimal source duration is 4.3 s. The vertical lines and black dots indicate the GLL points and the values ascribed to them.

Since we have already shown that the structural model is accurate, we attribute the discrepancies between the mainshock data and the point-source synthetics mostly to finite-source effects. This suggests that a finite-source inversion can indeed yield information about the kinematics of the Bárdarbunga caldera drop.

5. Probabilistic finite source inversion

The solutions of kinematic source inversions are known to be highly non-unique due to the limited amount of data and the presence of noise (e.g. Monelli and Mai, 2008). For this reason we decided to implement a probabilistic inversion that is based on a random exploration of the model parameter space (e.g. Tarantola, 2005).

5.1. Inversion setup

5.1.1. Finite fault parameterisation

Our finite fault model contains a deliberately small number of parameters. This facilitates the identification of the essential aspects of the rupture process, and it permits a sufficiently dense sampling of the parameter space.

We subdivide the ring fault into 10 regularly spaced subfaults, as is common in finite source studies (e.g. Hartzell and Heaton, 1993; Cotton and Campillo, 1995). The surface trace of the fault is inferred from satellite images (ASTER Volcano Archive, http://ava.jpl.nasa.gov), gravity anomalies (Gudmundsson and Högnadóttir, 2007) and the distribution of aftershock hypocentres (Konstantinou et al., 2000; Icelandic Meteorological Office).

We set the depth of each fault segment to 2 km, acknowledging that the true depth extent of the rupture is neither known from independent sources nor resolvable by our data. The lack of vertical resolution on the fault results in uncertain estimates of the displacement along the fault segments. This is because the seismic waveforms mostly depend on the moment magnitudes of the individual segments, i.e. on the product of the displacement and the subfault area that ruptured. For this reason we decided to effectively invert for the subfault moment magnitudes. They are less affected by the unknown subfault depth extent, but still indicate the amount of elastic energy radiated from the individual segments.

Since analogue experiments (e.g. Roche et al., 2001; Cole et al., 2005) indicate that ring fault structures may not be strictly outward dipping, we allow the inclination of the fault segments to attain values of -15° (inward dipping), 0° or $+15^\circ$ (outward dipping). This discretisation is intended to cover the range of inclination angles observed in field studies and analogue experiments. While a finer discretisation is technically possible, this would not be meaningful due to the limited resolution with respect to the subfault dip. The rupture process on each subfault is specified by a local rupture time and a local displacement that we assume to be downwards along the fault. We fix the rise time on each segment to 1 s, instead of keeping it variable. This restriction of the model space can be justified by two arguments: (1) The rise time is generally smaller than the total source duration of about 5 s (Nettles and Ekström, 1998; section 4), and (2) the shortest period used in the inversion is also 5 s, so that variations of the rise time do not affect the waveforms sufficiently much to be detectable. For each subfault we compute numerical Greens functions that are then combined with a specific parameter set to yield synthetic displacement velocities at the receiver sites (Cotton and Campillo, 1995).

5.1.2. Prior and marginal probability densities

As prior probability density functions (PDFs) we use Gaussian probability densities of order 1 that are induced by the L_1 norm (Tarantola, 2005). This choice is again motivated by the relative robustness of the L_1 norm. To obtain interpretable results, we compute

marginal PDFs via a Monte Carlo integration that is based on 10 million randomly generated finite fault models.

5.1.3. Data

For the finite source inversion we use three-component data. Since we were able to confirm the accuracy of the structural model only for vertical-component waveforms, we exclude horizontal-component waveforms where the influence of noise is visibly too high and where the moment tensor inversion indicates that the structural model may be too inaccurate. This selection process is, unavoidably, subjective. The data weighting is done as follows: (1) Weights are inversely proportional to the epicentral distance and designed to compensate for the uneven azimuthal coverage. This part of weighting scheme is the same as in the verification of the structural model using aftershock data. (2) Horizontal-component data that are not excluded from the inversion are down-weighted by a factor of 0.3 relative to the vertical-component data. This is because the horizontal components are generally noisier and more difficult to model accurately. (3) Where they are clearly identifiable, body waves are up-weighted by a factor of 2 in order to reduce the non-uniqueness of the finite source inversion. (4) Data from the three frequency bands already used for the moment tensor inversion are weighted equally. This also improves the resolution of the rupture models, as was shown by Mendoza and Hartzell (1988).

In a series of tests we modified the weighting scheme in order to assess its effect on the inversion results. Up-weighting the body wave part of the seismograms proved to be crucial. This is expected because surface waves from shallow sources are known to poorly constrain the source mechanism (e.g. Dziewonski et al., 1981). Changes in the epicentral distance weighting only affected the fine details of the posterior probability densities. The maximum likelihood models, however, are robust and hardly sensitive to the epicental distance weighting.

Since current tomographic models generally do not predict the amplitudes of seismic waves (Tibuleac et al., 2003; Bozdağ and Trampert, 2009), we normalised all observed and synthetic seismograms to a maximum amplitude of 1. The normalisation is done station by station in order to keep the relative amplitude of each component. This normalisation implies that we can only invert for the relative magnitude of an individual subfault rupture with respect to the magnitudes on the other subfault ruptures. We thus obtain information about the relative energies radiated from the fault segments.

6. Results

In Figs. 6–8 we present the marginal probability densities for the parameters rupture time, relative magnitude and inclination angle on the different subfaults. The probability densities are shown in the form of histograms, where the height of each bar indicates the probability that a given parameter falls into the interval covered by the width of that bar. Gray bars in the histograms indicate the most probable model, the synthetic waveforms of which are plotted in Fig. 9 together with the observed waveforms. As an interpretative aid, we also show the probability distributions as gray scale images plotted in circular form in the centres of Figs. 6–8. Light colours represent high probabilities and dark colours low probabilities. In the following paragraphs, we focus on the principal properties of the probability distributions. A more detailed analysis is possible but hard to justify given the uncertain influence of noise and possible inaccuracies of the structural model.

The PDFs for the rupture time, shown in Fig. 6, indicate that the rupture is likely to have initiated in the north-western part of the ring fault. This is where the PDFs attain a well-defined maximum between 1 s and 2 s prior to the reference time. Towards the eastern part of the ring fault the most likely rupture times are around 1 s later than the

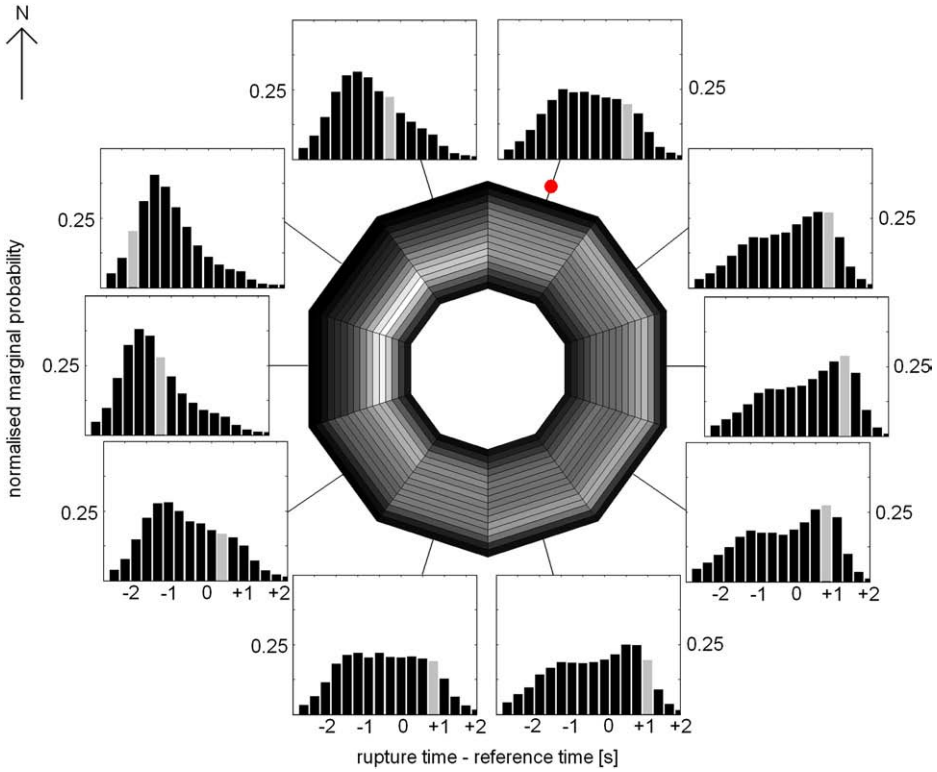

Fig. 6. Marginal probability distributions for the rupture time on the individual fault segments. The height of a bar in the histograms indicates the probability that the rupture time on a given segment falls into the interval covered by the width of that bar. The circular image in the centre shows the marginal probability densities as gray scale distributions. The rupture is likely to have initiated on the north-western segments. It spread to the remaining parts of the ring fault within probably less than 3 s. The rupture times for the most probable finite source model are represented by gray columns. A red dot marks the location of the aftershock used to verify the structural model.

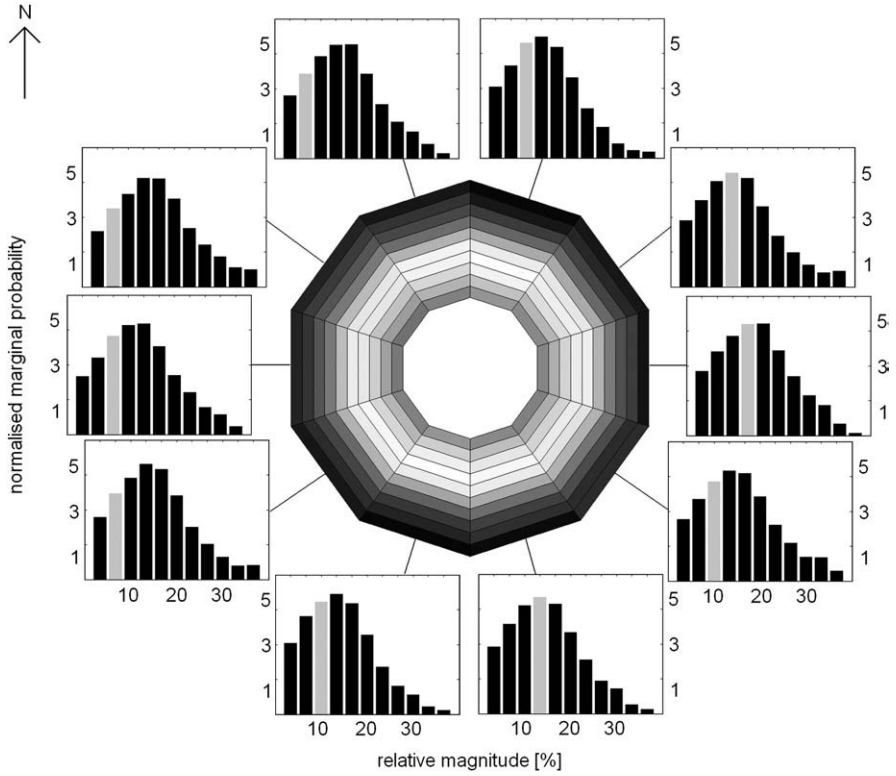

Fig. 7. Marginal probability densities for the relative magnitudes of the ring fault segments. Each of the 10 subfaults released about 10% of the total elastic energy. The relative magnitudes for the most probable finite source model are shown as gray columns.

reference time, but the maxima are less pronounced. We infer that the rupture spread around the ring fault in possibly less than 3 s. This is in agreement with an estimated total source duration of about 5 s.

The PDFs for the relative magnitudes (Fig. 7) show little variation between the individual fault segments. The maxima are clearly defined and collectively located between 10% and 15% of the total

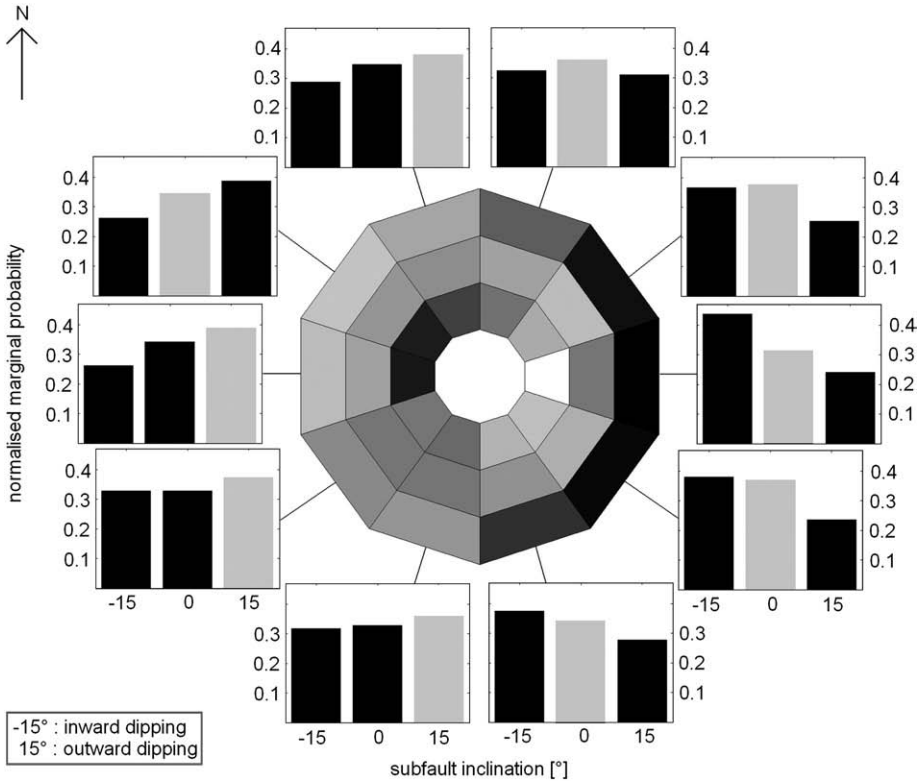

Fig. 8. Marginal probability densities for the subfault inclination angle. There is evidence that the western part of the ring fault is outward dipping while the inclination angle of the eastern part of the ring fault is probably closer to 0°. The subfault inclination angle for the most probable finite source model are shown as gray columns.

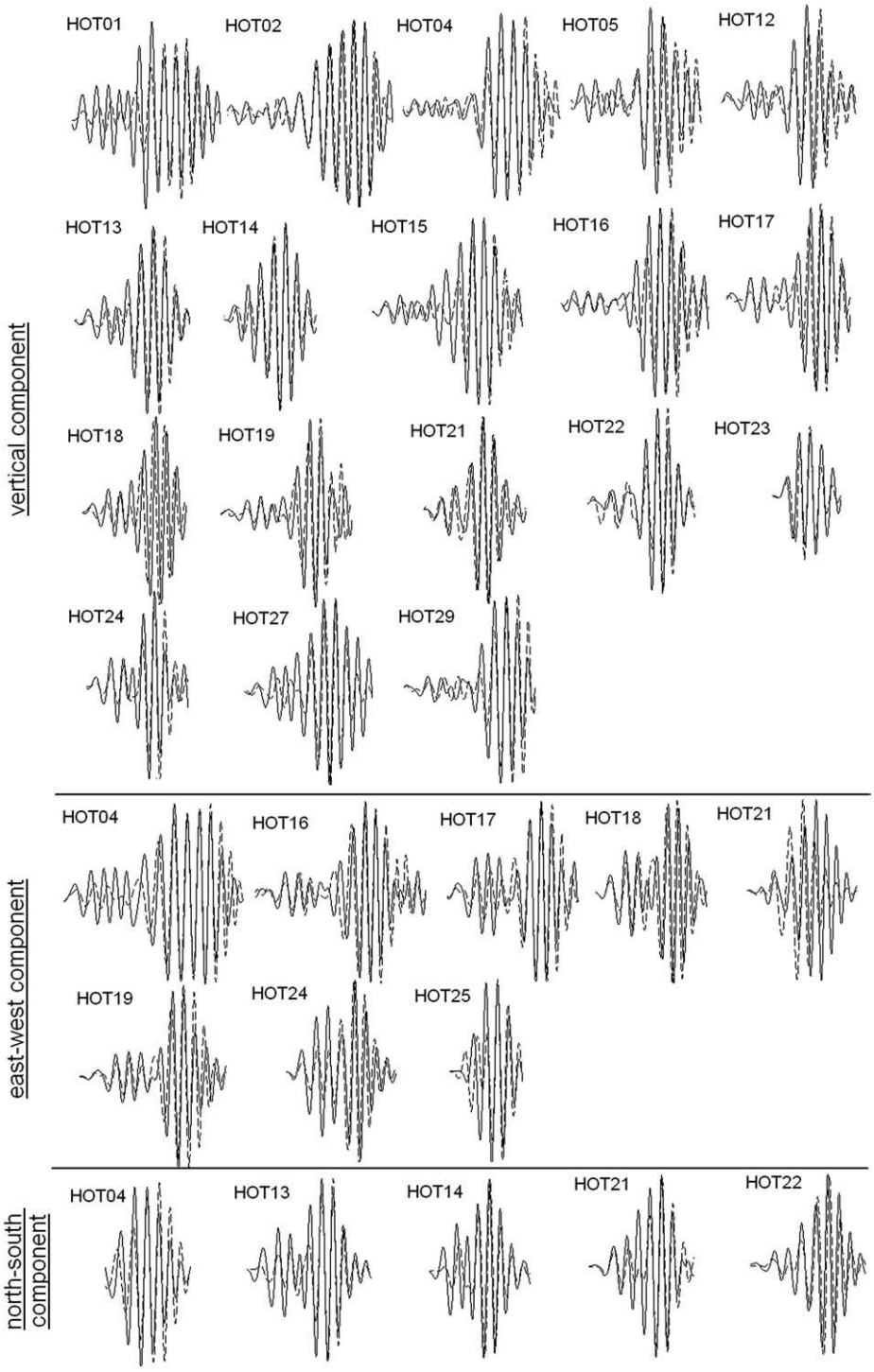

Fig. 9. Waveform comparison between the observed waveforms (solid curves) and the synthetic waveforms (dashed curves) for the most likely model, the source parameters of which are given in Figs. 6–8. The dominant period is 5 s.

magnitude. This indicates that each subfault radiated approximately the same amount of seismic energy. There is, moreover, no obvious relation between the rupture time and the relative magnitude.

Fig. 8 suggests that the constraints on the subfault inclination are weaker than the constraints on the rupture time and the relative magnitude. This is because the probabilities for the three different inclination angles do not deviate much from the value 0.33. There is, nevertheless, a clear preference for outward-dipping segments in the eastern part and inward-dipping or vertical segments in the western part of the ring fault.

The parameters of the most probable model, visualised in the form of gray bars in the histograms of Figs. 6–8, are mostly close to the maximum likelihood values. This suggests that the global PDF is dominated by a single maximum rather than being strongly multi-modal. The most probable rupture scenario is characterised by (1) the initiation in the north-western part of the ring fault, (2) the radiation of about 10% of the total elastic energy by each of the segments and (3) a subfault inclination that is outward-dipping in the western part and vertical in the eastern part of the ring fault. Fig. 9 summarises the waveform fit generated by the most likely model in the frequency

band around 0.2 Hz. Notable discrepancies between the observed and synthetic waveforms are mostly limited to the early parts of the wavetrains. An improvement relative to the optimal point source (Fig. 4) is clearly visible.

7. Discussion

We performed a kinematic source inversion for the September 29, 1996, Bárdarbunga earthquake. Our method is based on (1) the discretisation of the caldera ring fault, (2) the computation of numerical Greens functions for a 3D model of the Icelandic crust and uppermost mantle, and (3) a random exploration of the model space that yields marginal probability density functions for the finite rupture parameters. In the following paragraphs we discuss technical details of the inversion and we interpret the results in terms of the kinematics of the caldera drop at Bárdarbunga volcano.

The best resolved feature of the finite source inversion is the initiation of the rupture in the north-western part of the ring fault (Fig. 6). This is in agreement with the hypocentre location. From the initiation point, the rupture spread to the remaining fault segments within about 3 s. The rupture on a specific fault segment can thus not have been triggered exclusively by the rupture on neighbouring fault segments. This is because the propagation speed along the ring fault of about 6 km/s would be close to or in excess of the P wave speed in the upper crust which is about 5.5 km/s. The most plausible explanation for this phenomenon is that the rupture on different fault segments was not caused by the rupture propagation along the ring fault but by the propagation of seismic P waves across the caldera. We therefore do not require super-shear rupture in the classical sense, as it has been observed on planar faults (e.g. Bouchon and Vallée, 2003; Dunham and Archuleta, 2004). Tkalčić et al. (2005) and Dreger et al. (2005) also formulated this hypothesis on the basis of a forward modelling study where various caldera geometries were tested and finite difference modelling in composite 1D models was used to produce synthetic data.

The probability density functions for the relative magnitudes on the fault segments, shown in Fig. 7, suggest that the subfaults radiated nearly equal amounts of seismic energy. We therefore hypothesise that the caldera dropped uniformly as one coherent block. It appears unlikely that the caldera subsided asymmetrically. Similar relative magnitudes moreover indicate that there are no locked fault segments.

The inclination angle of the subfault segments is less well constrained than the rupture times and relative magnitudes. There is nevertheless a clear preference for outward-dipping segments in the western and inward-dipping or vertical segments in the eastern part of the ring fault. Our results indicate that the geometry of the fault is more complex than a simple outward-dipping cone. Since the rupture is likely to have occurred on a pre-existing ring fault, its current shape reflects the conditions at the time of its formation. Factors contributing to the ring fault irregularity include an irregularly shaped magma chamber, an anisotropic stress field or structural heterogeneities.

The assumption that the rupture occurred on one single ring fault is necessary in order to keep the number of free parameters sufficiently small for the limited amount of available data. While this simplification can be justified with Occam's razor, analogue experiments indicate that multiple faults may develop when the geometry of the magma chamber is complex (Acocella et al., 2001) or when the aspect ratio of the magma chamber roof (height/width) is greater than 1 (Roche et al., 2000). At least a high roof aspect ratio can be excluded based on gravity data (Gudmundsson and Högnadóttir, 2007). The lack of information on the fault geometry, especially at depth, is a general dilemma in finite source inversion that may only in the future be overcome with the help of more detailed geological observations and more abundant seismic data.

A particularity of the 1996 Bárdarbunga event is the occurrence of the major eruption after the September 29 earthquake. This apparent contradiction to a caldera drop induced by underpressure in the magma chamber, allowed Konstantinou et al. (2003) to argue for pre-eruptive fluid injection as a likely source mechanism. Their hypothesis is, however, inconsistent with the locations of aftershocks along the caldera rim. Nettles and Ekström (1998) proposed a modified version of a caldera drop where the inflation of a shallow magma chamber may cause rupture on ring faults below the chamber. While this scenario seems possible, we note that a caldera drop prior to the major eruption is consistent with petro-chemical data and a classical geometry where the ring fault is located above the magma chamber. Martí et al. (2000) demonstrated that the eruption of only a few percent of the total magma chamber content may trigger a caldera collapse. The same conclusion was reached by Druitt and Sparks (1984). A minor subglacial eruption under the 400 m to 600 m thick ice sheet would, however, not have been observable at the surface. There is, thus, no observational evidence against a small-scale eruption prior to the caldera drop that caused the September 29 earthquake. The caldera drop could then have increased the pressure inside the chamber from magmastatic to lithostatic, thus inducing the principal eruption (Martí et al., 2000). Additional caldera subsidence in the course of the principal eruption occurred through smaller earthquakes along the ríng fault structure.

It is, in this context, important to note that the finite source inversion of the Bárdarbunga earthquake captures an episode of a longer cycle that involves repeated caldera uplift and possibly more than one modes of caldera subsidence. Deformation processes occurring on either longer time scales or along smaller fault segments can not be constrained with the currently available data.

8. Conclusions

The accurate modelling and prediction of volcanic eruptions depends critically on information concerning the interaction between the caldera and the underlying magma chamber. Knowledge concerning the kinematics of a caldera in the course of an eruption is therefore essential. Uplift and subsidence of a volcanic caldera occur on different time scales; and for time scales from around 0.1 s to several tens of seconds, seismology provides efficient analysis tools.

We have shown that seismic data from a sufficiently dense broadband network can be used to constrain the kinematics of a volcanic caldera drop. This is intended to aid in the future design of realistic models of volcano dynamics that are then required to satisfy the constraints imposed by finite seismic source inversions.

The use of highly accurate numerical simulations of seismic wave propagation through realistically heterogeneous Earth models is an essential ingredient of the finite-source inversion presented above. This is because the Icelandic crust and upper mantle are complex and because finite-source effects are small when the epicentral distance exceeds the characteristic length scale of the source, which is about 10 km in our case.

Further progress in our understanding of caldera kinematics will therefore depend critically on the installation of seismic stations in the closer vicinity of volcanic centres, that is at distances on the order of the caldera diameter. These new stations should ideally produce usable data at periods that correspond to wavelengths that are a suitable fraction (intuitively 1/5 to 1/2) of the caldera circumference. Equally important are more accurate structural models and larger computational resources that allow us to account for structural complexities in the simulation of seismic wave propagation.

For future studies we envision a direct link between seismologically constrained caldera movement, volcanic edifice deformation and magma chamber processes. The work presented here is a first step towards this goal.

8. Acknowledgements

We thank the German Academic Exchange Service (DAAD) for financial support. Discussions with members of the volcanology

groups at Munich University and The Australian National University helped us to improve the manuscript.

References

Acocella, V., Cifelli, F., Funicello, R., 2001. Formation and architecture of nested collapse calderas: insights from analogue models. Terra Nova 13, 58–63.

Acocella, V., 2007. Understanding caldera structure and development: An overview of analogue models compared to natural calderas. Earth-Science Reviews 85, 125–160.

Allen, R.M., Nolet, G., Morgan, W.J., et al., 2002. Imaging the mantle beneath Iceland using integrated seismological techniques. Journal of Geophysical Research 107 (B12). doi:10.1029/2001JB000595.

Båth, M., 1960. Crustal structure of Iceland. Journal of Geophysical Research 65 (6), 1793–1807.

Bouchon, M., Vallée, M., 2003. Observation of long supershear rupture during the magnitude 8.1 Kunlunshan earthquake. Science 301, 824–826.

Bozdağ, E., Trampert, J., 2009. Assessment of tomographic mantle models using spectral element seismograms. Geophysical Journal International, submitted.

Branney, M.J., 1995. Downsag and extension at calderas: new prospectives on collapse geometries from ice-melt, mining and volcanic subsidence. Bulletin of Volcanology 57, 303–318.

Cole, J.W., Milner, D.M., Spinks, K.D., 2005. Calderas and caldera structures: a review. Earth Science Reviews 69, 1–26.

Cotton, F., Campillo, M., 1995. Frequency domain inversion of strong motions: Application to the 1992 Landers earthquake. Journal of Geophysical Research 100, 3961–3975.

Darbyshire, F.A., Bjarnason, I.T., White, R.S., Flóvenz, Ó., 1998. Crustal structure above the Iceland mantle plume imaged by the ICEMELT refraction profile. Geophysical Journal International 135, 1131–1149.

Dreger, D., Tkalčić, H., Foulger, G., Julian, B., 2005. Kinematic Modeling and Complete Moment Tensor Analysis of the Anomalous, Vertical CLVD Bardarbunga, Iceland, Event. Eos Transaction AGU, 86(52), Fall Meeting Supplement, Abstract S33C–08, San Francisco.

Druitt, T.H., Sparks, R.S.J., 1984. On the formation of calderas during ignimbrite eruptions. Nature 310, 679–681.

Du, Z., Foulger, G.R., 2001. Variation in the crustal structure across central Iceland. Geophysical Journal International 145, 246–264.

Du, Z., Foulger, G.R., Julian, B.R., 2002. Crustal structure beneath western and eastern Iceland from surface waves and receiver functions. Geophysical Journal International 149, 349–363.

Du, Z., Foulger, G.R., 2004. Surface wave waveform inversion for variation in upper mantle structure beneath Iceland. Geophysical Journal International 157, 305–314.

Dunham, E.M., Archuleta, R.J., 2004. Evidence for a supershear transient during the 2002 Denali earthquake. Bulletin of the Seismological Society of America 94, 256–268.

Dziewonski, A.M., Chou, T.-A., Woodhouse, J.H., 1981. Determination of earthquake source parameters from waveform data for studies of global and regional seismicity. Journal of Geophysical Research 86, 2825–2852.

Ekström, G., 1994. Anomalous earthquakes on volcano ring-fault structures. Earth and Planetary Science Letters 128, 707–712.

Fichtner, A., Igel, H., 2008. Efficient numerical surface wave propagation through the optimisation of discrete crustal models - a technique based on non-linear dispersion curve matching (DCM). Geophysical Journal International 173, 519–533.

Folch, A., Martí, J., 2009. Time-dependent chamber and vent conditions during explosive caldera-forming eruptions. Earth and Planetary Science Letters 280, 246–253.

Foulger, G.R., Pritchard, M.J., Julian, B.R., et al., 2001. Seismic tomography shows that upwelling beneath Iceland is confined to the upper mantle. Geophysical Journal International 146, 504–530.

Foulger, G.R., Du, Z., Julian, B.R., 2003. Icelandic-type crust. Geophysical Journal International 155, 567–590.

Geshi, N., Shimano, T., Chiba, T., Nakada, S., 2002. Caldera collapse during the 2000 eruption of Miyakejima Volcano, Japan. Bulletin of Volcanology 64, 55–68.

Geyer, A., Folch, A., Martí, J., 2006. Relationship between caldera collapse and magma chamber withdrawal: An experimental approach. Journal of Volcanology and Geothermal Research 157, 375–386.

Graves, R.W., Wald, D.J., 2001. Resolution analysis of finite fault source inversion using one- and three-dimensional Greens functions, 1. Strong motions. Journal of Geophysical Research 106, 8745–8766.

Gudmundsson, M.T., Högnadóttir, T., 2007. Volcanic systems and calderas in the Vatnajökull region, central Iceland: Constraints on crustal structure from gravity data. Journal of Geodynamics 43, 153–169.

Hartzell, S.H., Heaton, T.H., 1993. Inversion of strong ground motion and teleseismic waveform data for the fault rupture history of the 1979 Imperial Valley, California earthquake. Bulletin of the Seismological Society of America 73, 1553–1583.

Kirkpatrick, S., Gelatt, C.D., Vecchi, M.P., 1983. Optimization by Simulated Annealing. Science 220, 671–680.

Konstantinou, K.I., Nolet, G., Morgan, W.J., Allen, R.M., Pritchard, M.J., 2000. Seismic phenomena associated with the 1996 Vatnajökull eruption, central Iceland. Journal of Volcanology and Geothermal Research 102, 169–187.

Konstantinou, K.I., Kao, H., Lin, C.-H., Liang, W.-T., 2003. Analysis of broad-band regional waveforms of the 1996 September 29 earthquake at Bárdarbunga volcano, central Iceland: investigation of the magma injection hypothesis. Geophysical Journal International 154, 134–145.

Martí, J., Folch, A., Neri, A., Macedonio, G., 2000. Pressure evolution during explosive caldera-forming eruptions. Earth and Planetary Science Letters 175, 275–287.

Mendoza, C., Hartzell, S.H., 1988. Inversion for slip distribution using teleseismic P waveforms: North Palm Springs, Borah Peak, and Michoacan earthquakes. Bulletin of the Seismological Society of America 78, 1092–1111.

Monelli, D., Mai, P.M., 2008. Bayesian inference of kinematic earthquake rupture parameters through fitting of strong motion data. Geophysical Journal International 173, 220–232.

Mori, J., McKee, C., 1987. Outward-dipping ring-fault structure at Rabaul caldera as shown by earthquake locations. Science 235, 193–195.

Mori, J., White, R., Harlow, D., Okubo, P., Power, J., Hoblitt, R., Laguerta, E., Lanuza, L., Bautista, B., 1996. Volcanic earthquakes following the 1991 climatic eruption of Mount Pinatubo, Philippines: strong seismicity during a waning eruption. In: Newhall, C., Punongbayan, R. (Eds.), Fire and Mud: Eruptions and Lahars of Mount Pinatubo. PHIVOLCS and Univ. Washington Press, Philippines, pp. 339–350.

Nettles, M., Ekström, G., 1998. Faulting mechanism of anomalous earthquakes near Bárdarbunga Volcano, Iceland. Journal of Geophysical Research 103, 17,973–17,983.

Prejean, S., Stork, A., Ellsworth, W., Hill, D., Julian, B., 2003. High precision earthquake locations reveal seismogenic structure beneath Mammoth Mountain California. Geophysical Research Letters 30. doi:10.1029/2003GL018334.

Roche, O., Druitt, T.H., Merle, O., 2000. Experimental study of caldera formation. Journal of Geophysical Research 105, 395–416.

Roche, O., van Wyk de Vries, B., Druitt, T.H., 2001. Sub-surface structures and collapse mechnisms of summit pit craters. Journal of Volcanology and Geothermal Research 105, 1–18.

Rymer, H., van Wyk de Vries, B., Stix, J., Williams-Jones, G., 1998. Pit crater structure and processes governing persistent activity at Masaya Volcano, Nicaragua. Bulletin of Volcanology 59, 345–355.

Scandone, R., Malone, S.D., 1985. Magma supply, magma discharge and readjustment of the feeding system of Mount St. Helens during 1980. Journal of Volcanology and Geothermal Research 23, 239–262.

Staples, R.K., White, R.S., Bransdóttir, B., et al., 1997. Färoe-Iceland Ridge Experiment - 1 Crustal structure of northeastern Iceland. Journal of Geophysical Research 102, 7849–7866.

Tarantola, A., 2005. Inverse problem theory and methods for model parameter estimation. Society of Industrial and Applied Mathematics, Philadelphia.

Tibuleac, I.M., Nolet, G., Michaelson, C., Koulakov, I., 2003. P wave amplitudes in a 3D Earth. Geophysical Journal International 155, 1–10.

Tkalčić, H., Dreger, D., Foulger, G., Julian, B., 2005. Kinematic modeling and complete moment tensor analysis of the anomalous, vertical CLVD Bardarbunga, Iceland, event. IASPEI General Assembly, Santiago de Chile, Chile.

Tkalčić, H., Dreger, D.S., Foulger, G.R., Julian, B.R., 2009. The puzzle of the 1996 Bárdarbunga, Iceland earthquake: No volumetric component in the source mechnism. Bulletin of the Seismological Society of America 99, 3077–3085.

Tryggvason, E., 1962. Crustal structure of the Iceland region from dispersion of surface waves. Bulletin of the Seismological Society of America 52, 359–388.